Supporting Information

Two-dimensional Bandgap and Defect-state Energy Variations in InGaN-based Micro-LEDs

Dong-Su Ko,*[a] Sihyung Lee,[b] Jinjoo Park,[c] Soohwan Sul,[a] Changhoon Jung,[a] Dong-Jin Yun,[a] Mi Kyung Kim,[a] Jaewoo Lee,[a] Jun Hee Choi,[c] Seong Yong Park,[a] Munbo Shim,[b] Won-Joon Son, [b] and Se Yun Kim* [d]

[a]Analytical engineering group, Samsung Advanced Institute of Technology, Suwon 16678, Republic of Korea
[b]Data & Information Technology Center, Samsung Electronics, Hwaseong 18848, Republic of Korea
[c]Device Research Center, Samsung Advanced Institute of Technology, Suwon 16678, Republic of Korea
[d]Department of Materials Engineering and Convergence Technology, Gyeongsang National University, Jinju 52828, Republic of Korea

Corresponding authors: seyun@gnu.ac.kr; ds02.ko@samsung.com

Current Methods and their Limitations in Micro-LED Degradation Study

The principal causes of optical degradation in micro-LED devices include the net effects of the structural and chemical changes induced by B-IIP. To identify the changes in the chemical states, XPS was employed, which is notably sensitive to surface chemical and electronic structures. The XPS results, which reveal the core-level structures of Ga $2p_{3/2}$, N 1s, Ga LMN, Ga 3d, and the valence band (VB), are shown in Figure S1. The figure shows no considerable changes between the pristine and B-IIP regions for a total ion dose of 1×10^{14} ions/cm^2 (denoted as the low-dose B-IIP). This is because changes in the chemical state at doping concentrations below approximately 10^{17} atoms/cm^3 do not considerably affect the XPS spectra.[S1]

Raman spectroscopy was employed to identify changes in the crystal structural vibrations at the surface of the micro-LED device. The Raman spectra highlight the three significant peaks at 520, 567, and 733 cm^{-1} (Figure S2), which correspond with Si (the substrate), the E2 (high) mode of GaN, and the A1 (longitudinal optical, LO) mode of GaN, respectively. While the peak positions remained relatively stable, an increase in the B-ion concentration reduced the luminous intensity. This was accompanied by an increase in the FWHM of the E2 (high) and A1 (LO) modes of GaN. Such changes in the Raman spectral features, notably in the FWHM, indicate increased defect or impurity concentrations within the crystal structure.

ToF–SIMS is an efficient technique with the smallest detection limit, thereby making it adept at tracing atoms. It offers a good spatial resolution of ~100 nm in the lateral direction and depth resolution of 1 nm via sputtering, making it ideal for depth profiling to measure doping levels. It is effective in analyzing the lateral and depth dimensions. However, concerning low-dose B-IIP, B was detectable in the B-doped p-Si substrate (~10^{19} ions/cm^3), but not in the LED structure. This corresponds with the XPS and Raman analyses results, wherein B was only measurable at the high-dose B-IIP of 320 nm below the LED structure (Figures S3c and S3d). The depth profiles for high-dose B-IIP were also simulated using the SRIM program,[S2] which predicted B-ion penetration

to a depth of ~280 nm. This simulation result corresponds with the ToF–SIMS measurement findings, as shown in Figures S3 and S4.

High-resolution X-ray diffraction (HRXRD) analysis was employed to obtain detailed information on the InGaN-based LED layers on the surface, while focusing on the structural changes in the crystal. This was achieved through the 2ϑ–ω scanning of the GaN (002) layer in out-of-plane geometry. The HRXRD pattern in the 2ϑ range of 30–40° exhibited Bragg reflections of GaN (002), AlGaN (002), and InGaN (002), coupled with several interference fringes (Figure S5). The peaks around $2\vartheta \approx 33.3°$, 34.6°, and 35.6° corresponded with AlGaN (002), InGaN (002), and GaN (002), respectively.[S3] Although the XRD patterns for the pristine and low-dose B-IIP samples were similar, a considerable change was observed in the high-dose B-IIP sample around 2θ ≈ 34°. This indicated that the crystal structure of InGaN in the MQW underwent modifications owing to the formation of defects or strain under high-dose B-IIP conditions.

The impact of low-dose B-IIP is evident in the different optical luminescence characteristics. However, identifying the structural and chemical origins of these effects using conventional analytical techniques is challenging. The inability of current analytical methods in terms of detecting the subtle chemical, electronic, and crystal structural changes induced by the low-dose B-IIP suggests that their detection limits are not sensitive enough. This necessitates more precise analysis techniques to elucidate the mechanism of optical degradation and optimize the manufacturing conditions of IIP. Analytical TEM, combined with EDS and EELS, based on a Cs-corrected system, represents a highly specialized technique for observing microstructures and measuring chemical and electronic characteristics using a spatial resolution of <1 nm. Utilizing wide-angle solid-state detectors in XEDS and high-efficiency CMOS cameras in EELS considerably enhances chemical tracking capabilities, thereby facilitating atomic-scale chemical mapping. Despite these advances, determining the effects of low-dose B-IIP remains challenging, including using different analytical TEM techniques. XEDS and EELS failed to detect any considerable chemical and electronic structural changes in the p-GaN layer between the PR-protected region and low-dose B-IIP region (Figure S6). EELS did not detect B (Figure S6f). Hence, even the

3

detection limits of XEDS and EELS are insufficient to detect the ion concentration at low levels of B-IIP.

The changes in the crystal structure resulting from the collision and interaction of accelerated B ions during the IIP process were examined using selected area electron diffraction patterns (SADPs). Although the d-spacing of (002) in p-GaN (perpendicular to the IIP direction) was measured, no considerable changes were observed beyond the typical measurement error range (generally <3%) (Figure S7). However, subtle shifts were observed in the peak positions of the (000–6) satellite diffraction patterns in the SADPs of the MQW and multilayers. These shifts suggest a disruption in the crystallographic periodicity of the MQW and multilayers owing to atomic displacements, which correspond with the HRXRD results for high-dose B-IIP (Figure S5). Although HRXRD could detect changes in the crystal structure for both high- and low-dose B-IIPs, SADP analysis was particularly effective at identifying changes at the low-dose level. This enhanced sensitivity of SADP is attributed to its focus on a smaller area (a 100-nm-diameter circle), notably on the MQW and multilayers, which is contrary to the broader area (several hundred micrometers) assessed using HRXRD. However, although SADP identified changes in the crystal structure of the MQW, B-IIP-induced changes could not be identified in high-angle annular dark-field STEM (HAADF–STEM) images, with a spatial resolution of <80 pm (Figure S8). This limitation is owing to the small field of view (FOV) of HAADF–STEM. Hence, a comprehensive analysis of the distribution of shifting atomic positions requires a larger FOV, thereby encompassing the PR-protected and B-IIP regions.
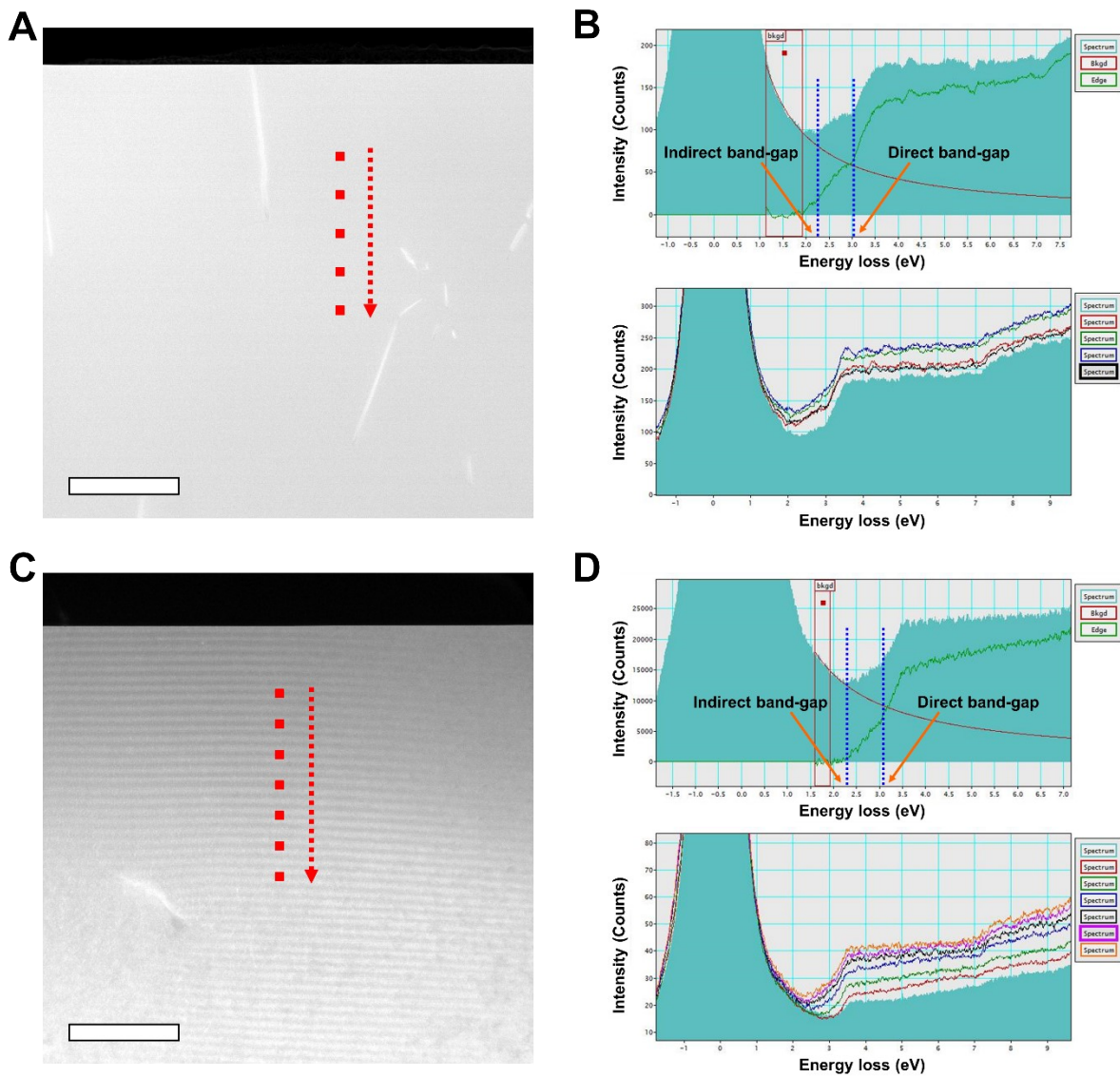
Figure S1. (a) and (c) HAADF–STEM images of GaN and the corresponding low-loss EELS spectra of the samples prepared using (b) Ar+ ion milling and (d) FIB, respectively. All scale bars are 50 nm.
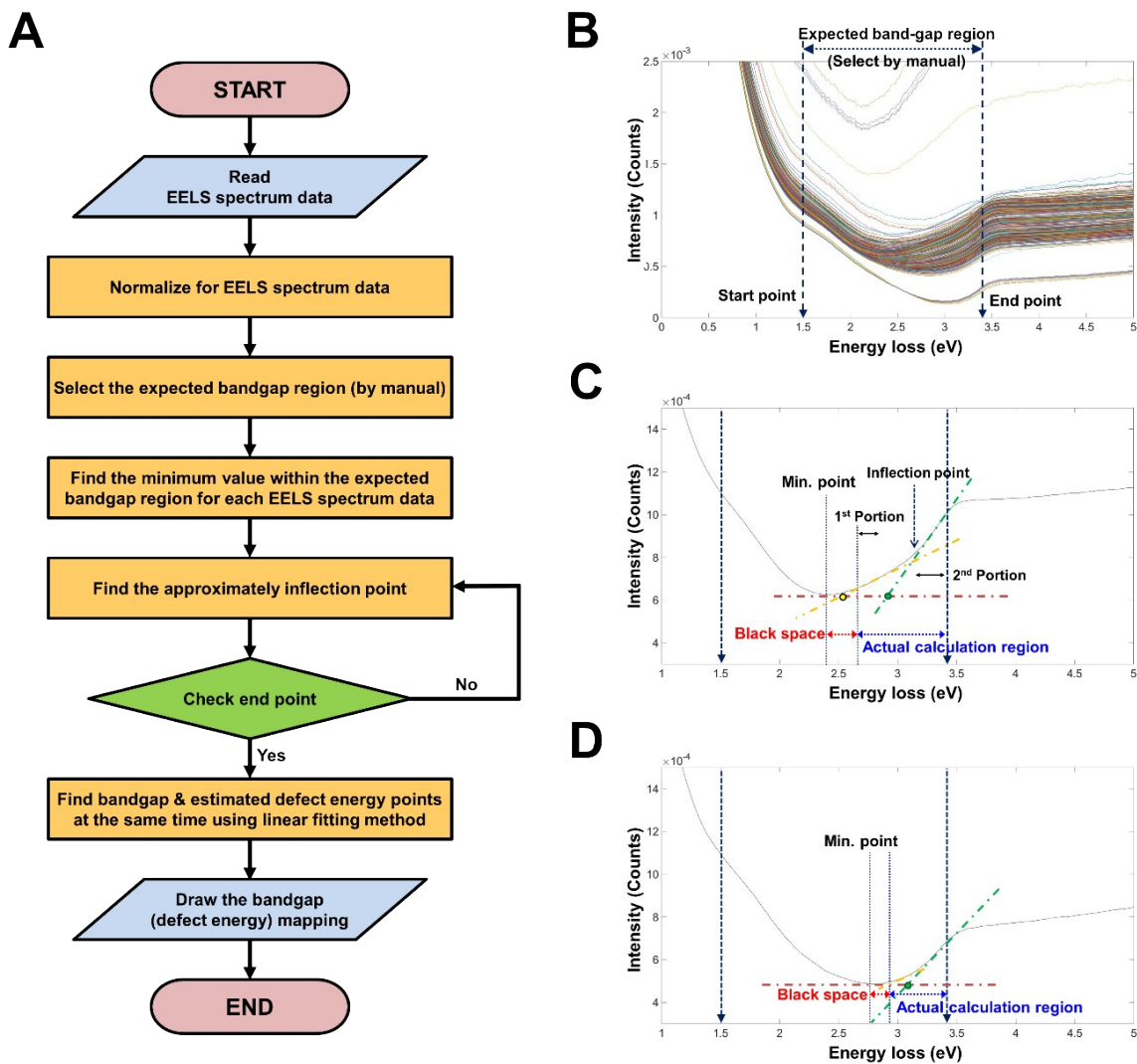
A

START

Read
EELS spectrum data

Normalize for EELS spectrum data

Select the expected bandgap region (by manual)

Find the minimum value within the expected
bandgap region for each EELS spectrum data

Find the approximately inflection point

Check end point

No

Yes

Find bandgap & estimated defect energy points
at the same time using linear fitting method

Draw the bandgap
(defect energy) mapping

END

B

C

D

Figure S2. (a) Flowchart of the linear fitting algorithm. (b) Manual process to determine the start and endpoints used for identifying the expected bandgap region from the full EELS spectral data. A typical spectrum for expecting (c) defect-state energy and (d) only bandgaps.
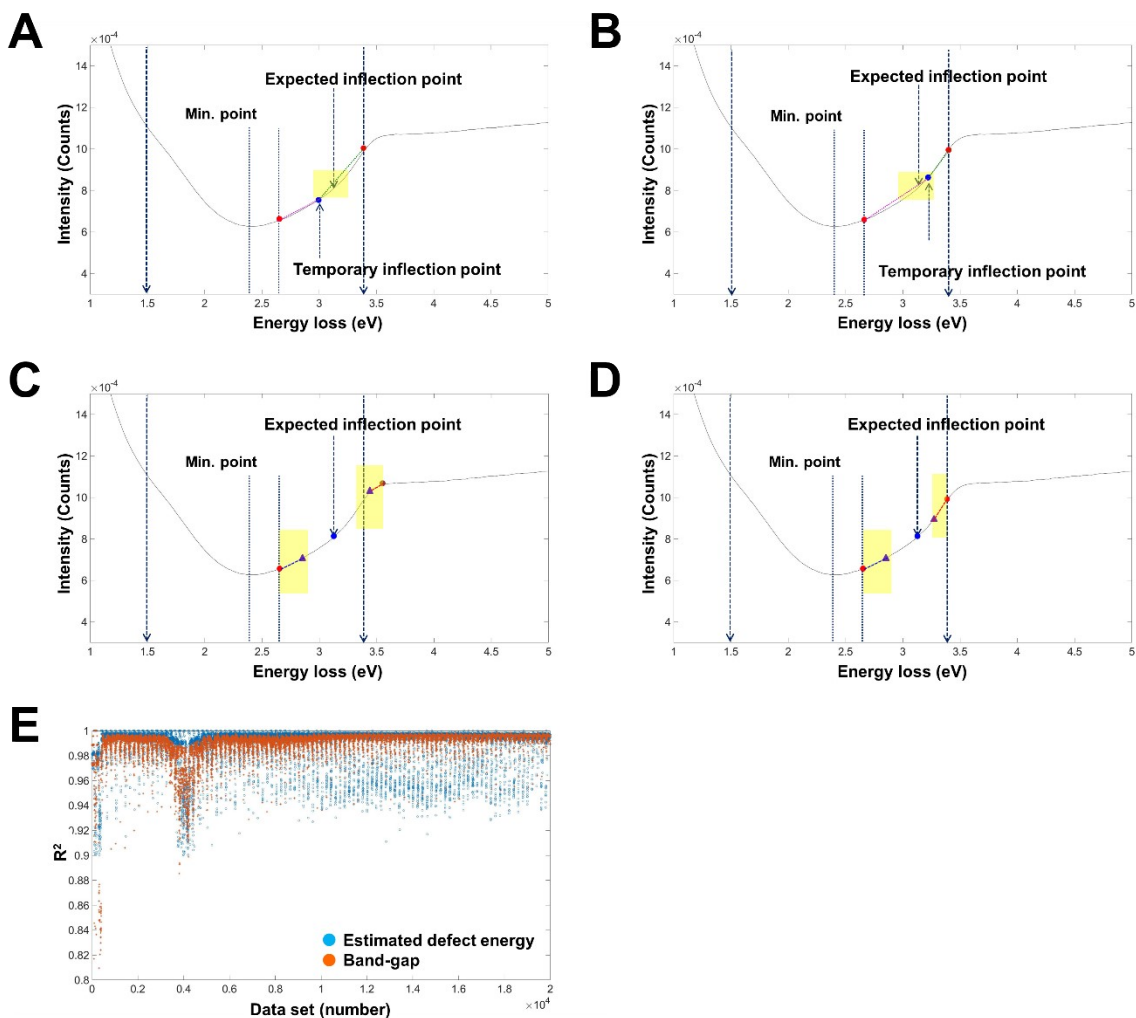
Figure S3. Method to identify the approximated inflection point in temporary inflection points (a) and (b) in the area represented in yellow. (c) If the endpoint, determined manually as shown in (b), is specified incorrectly, it would move in the negative direction of the x-axis and later reverse. (d) Accurate specification of the endpoint and (e) determination of the coefficient for all the data points within a certain range.
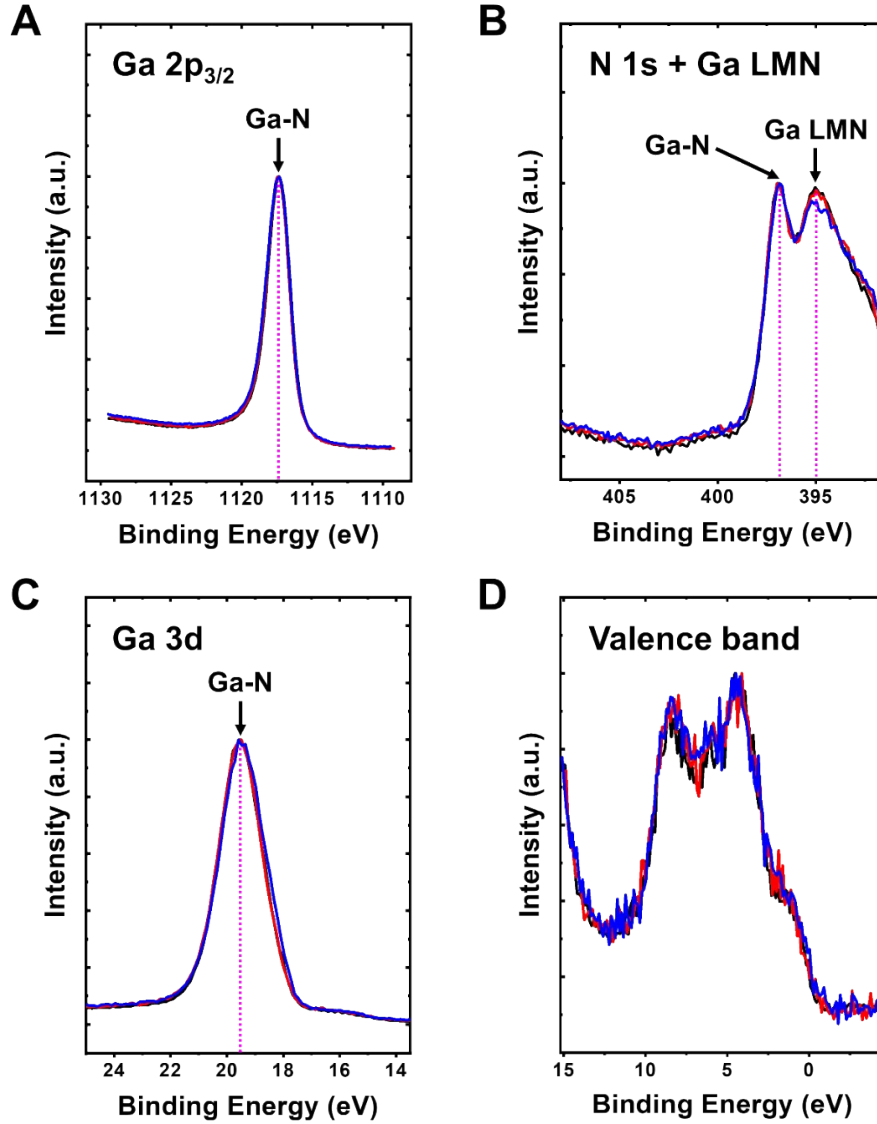
Figure S4. XPS spectra of (a) Ga 2p$_{3/2}$, (b) N 1s with Ga LMM, (c) Ga 3d, and (d) VB. The black line represents the pristine InGaN-based LED device; the red and blue ones represent InGaN-based LED devices with B-IIP performed at 80 keV with doses of 1×10^{14} and 1×10^{16} ions/cm^2, respectively.
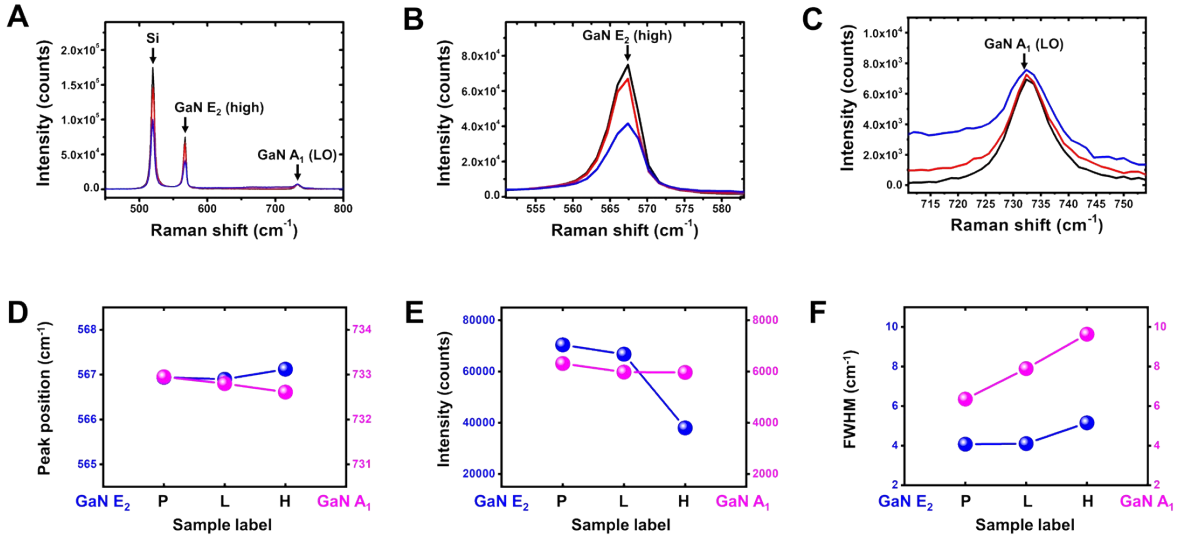
Figure S5. (a) Raman spectra of the B-IIP InGaN-based LED. (b) and (c) Enlarged spectra of E_2 and A^1 modes, respectively. The black line represents the pristine InGaN-based LED device, while the red and blue ones represent the InGaN-based LED devices with B-IIP performed at 80 keV with doses of 1×10^{14} and 1×10^{16} ions/cm^2, respectively. (d), (e), and (f) Changes in peak positions, intensity, and first width half maximum (FWHM) of the GaN E_2 and GaN A_1 modes, respectively (P represents the pristine InGaN-based LED device, while L and H B-IIP at 80 keV with total doses of 1×10^{14} and 1×10^{16} ions/cm^2, respectively).
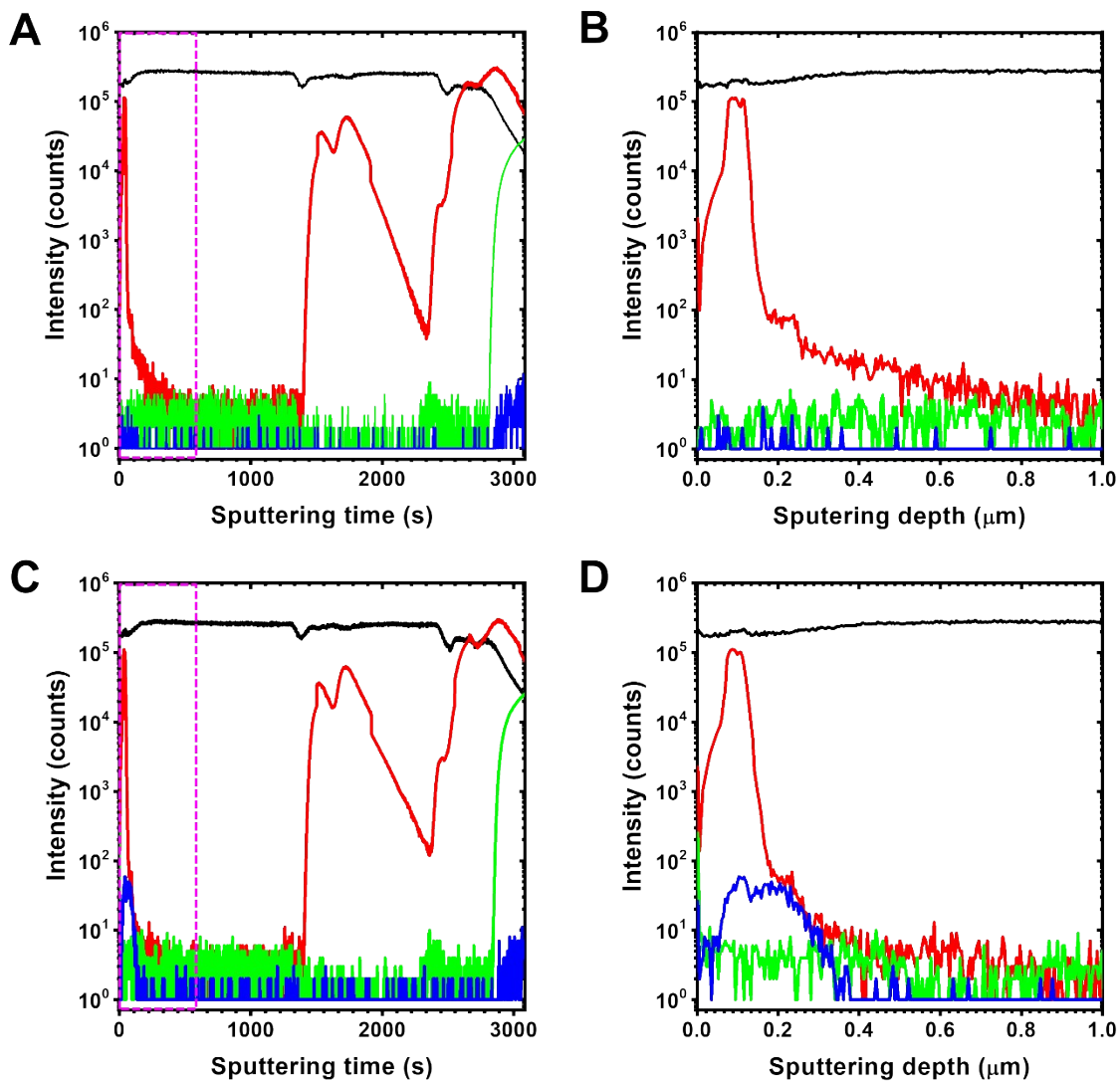
Figure S6. ToF–SIMS depth profiles of the B-IIP InGaN-based LED at 80 keV. (a,b) Total doses of 1×10^{14} ions/cm^2 and (c,d) 1×10^{16} ions/cm^2. X-axis unit is converted from (a) and (c) time to (b) and (d) depth. The black, red, green, and blue lines represent Ga, Al, Si, and B, respectively.

10
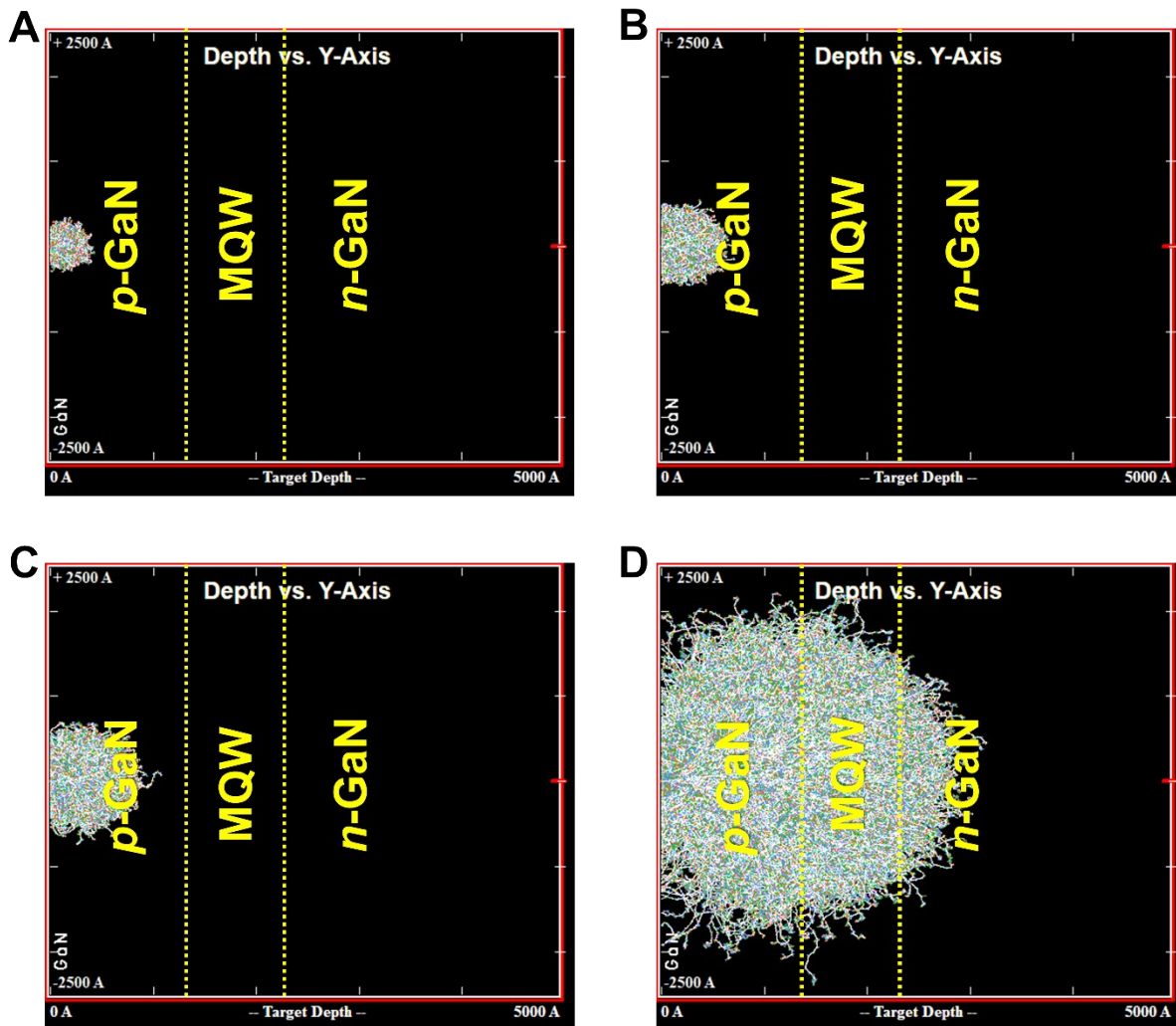
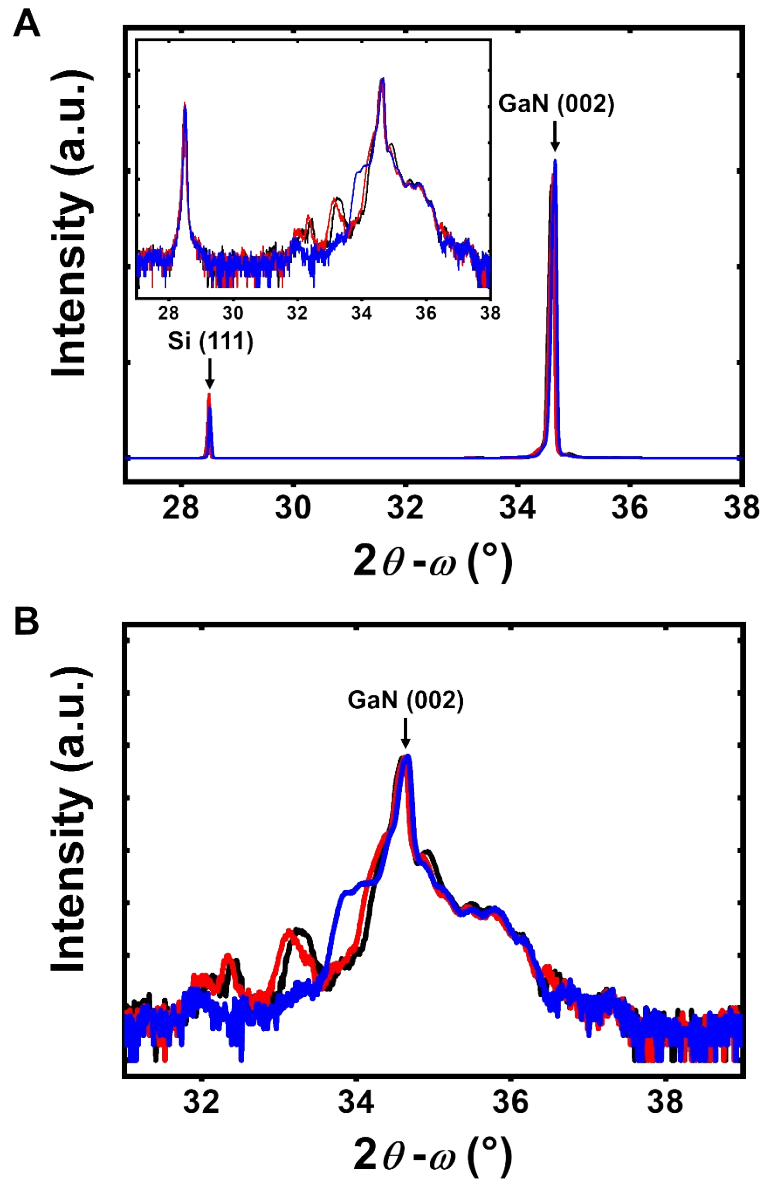**Figure S7.** SRIM simulation for B-IIP in GaN at beam energies of (a) 5 keV, (b) 10 keV, (c) 15 keV, and (d) 80 keV.

11

Figure S8. HRXRD 2θ-ω scans of the GaN (002) obtained in out-of-plane geometry. The black line represents the pristine InGaN-based LED device; the red and blue lines represent InGaN-based LEDs with B-IIP performed at 80 keV with doses of 1×10^{14} and 1×10^{16} ions/cm^2, respectively. Inset (a) is a logarithmic plot; (b) shows the corresponding enlarged plot.

12
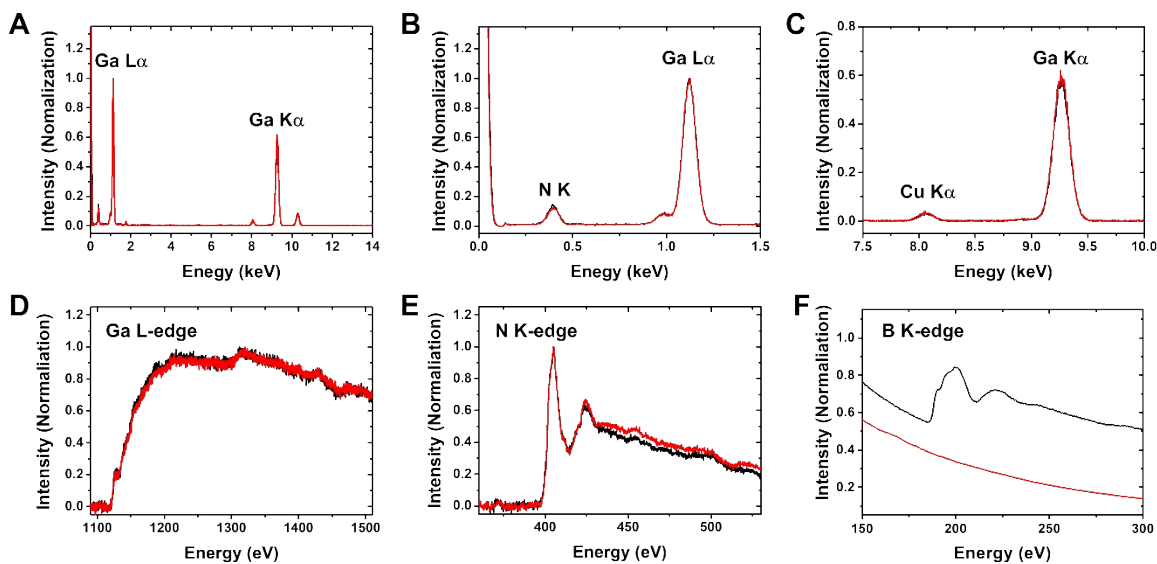
Figure S9. (a)–(c) XEDS profiles of low-dose B-IIP at *p*-GaN in the PR-protected and B-IIP regions. (d) Ga L-edge and (e) N K-edge EELS spectra of the low-dose B-IIP sample at *p*-GaN in the PR-protected and B-IIP regions. The black and red lines represent PR-protected and B-IIP regions, respectively. (f) B K-edge EELS spectra obtained from the Atlas reference (black line) and low-dose B-IIP sample (red line) at *p*-GaN in the B-IIP region.
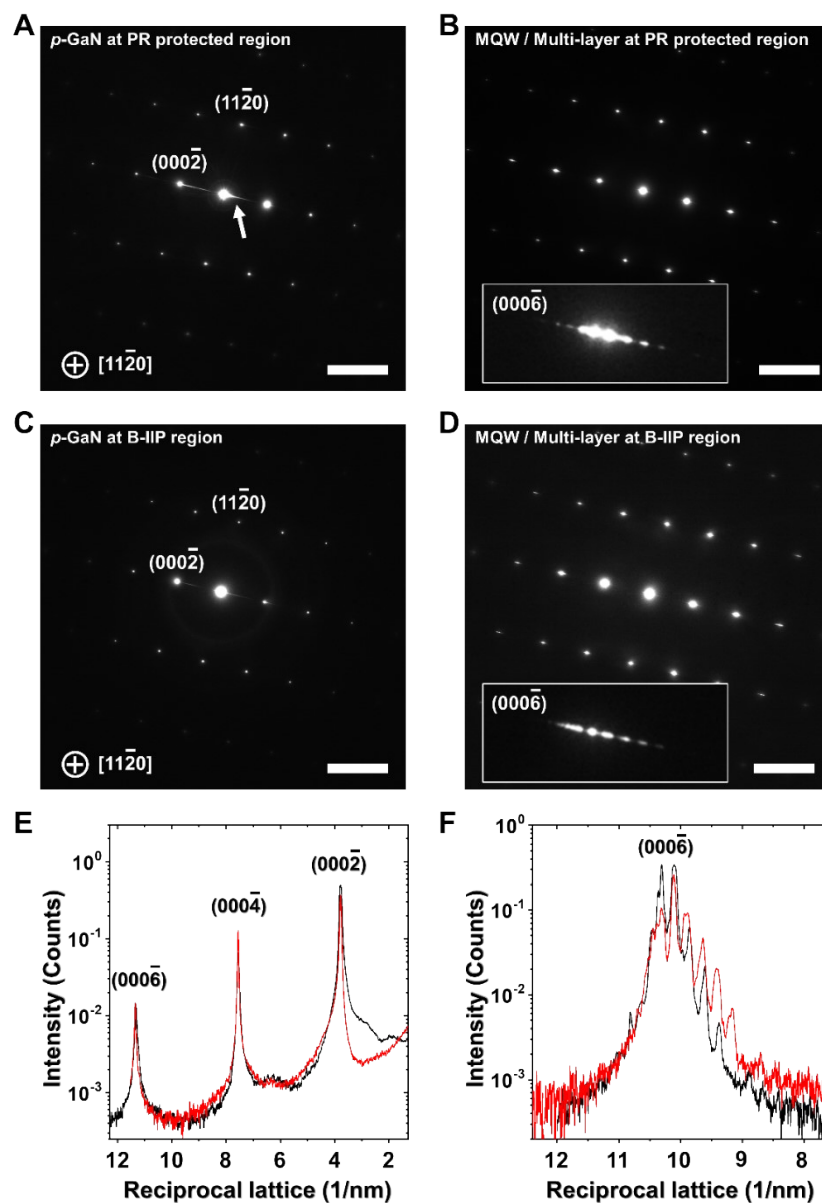
Figure S10. SADPs at the *p*-GaN and MQW/multilayer area in (a) and (b) PR-protected regions and (c) and (d) B-IIP regions, respectively. (e) Intensity line profiles of (a) and (b) in the horizontal direction of [0002]. (f) Intensity line profiles of (000-6) with satellite patterns in (b) and (d). Black and red lines represent the PR- and B-IIP regions, respectively. Streak lines represented by white arrows in (a) are the edge effects of TEM samples. All scale bars are 5 nm.
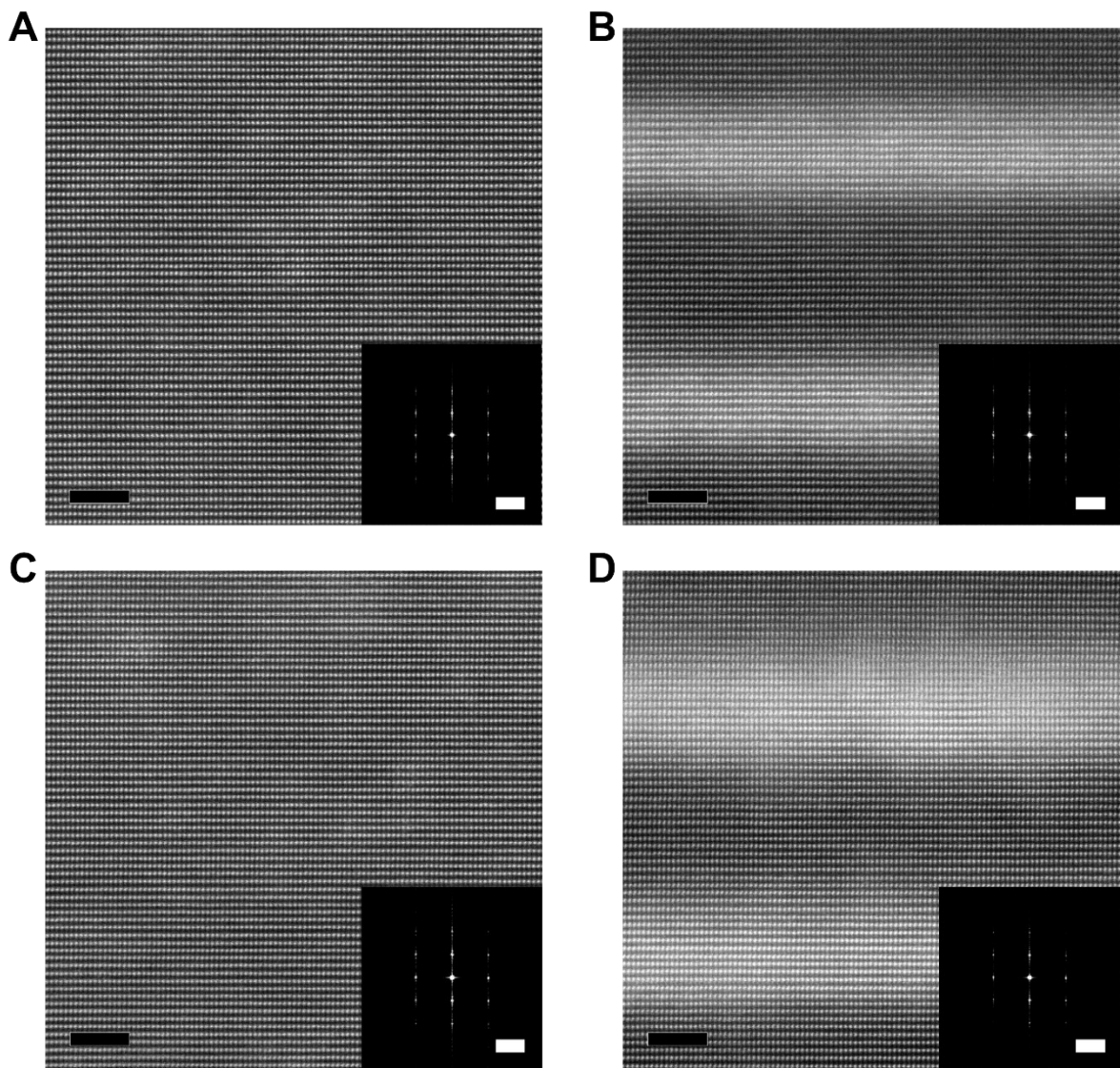
Figure S11. High-resolution HAADF–STEM images and corresponding fast Fourier transform images of a low-dose B-IIP sample at *p*-GaN and MQW/multilayer area in (a) and (b) PR-protected regions and (c) and (d) B-IIP regions, respectively. Scale bars of HAADF–STEM and FFT images are 2 nm and 5 nm^{-1}, respectively.
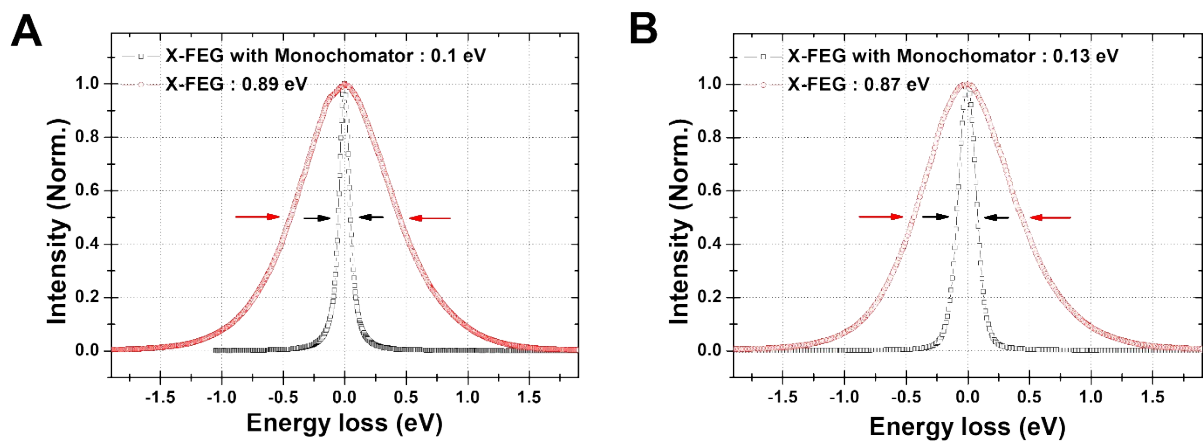
Figure S12. Zero-loss EELS spectra with an activated monochromator at (a) 80 and (b) 300 keV. The spectral resolution of the EELS measurement is determined by FWHM of the zero-loss peak.
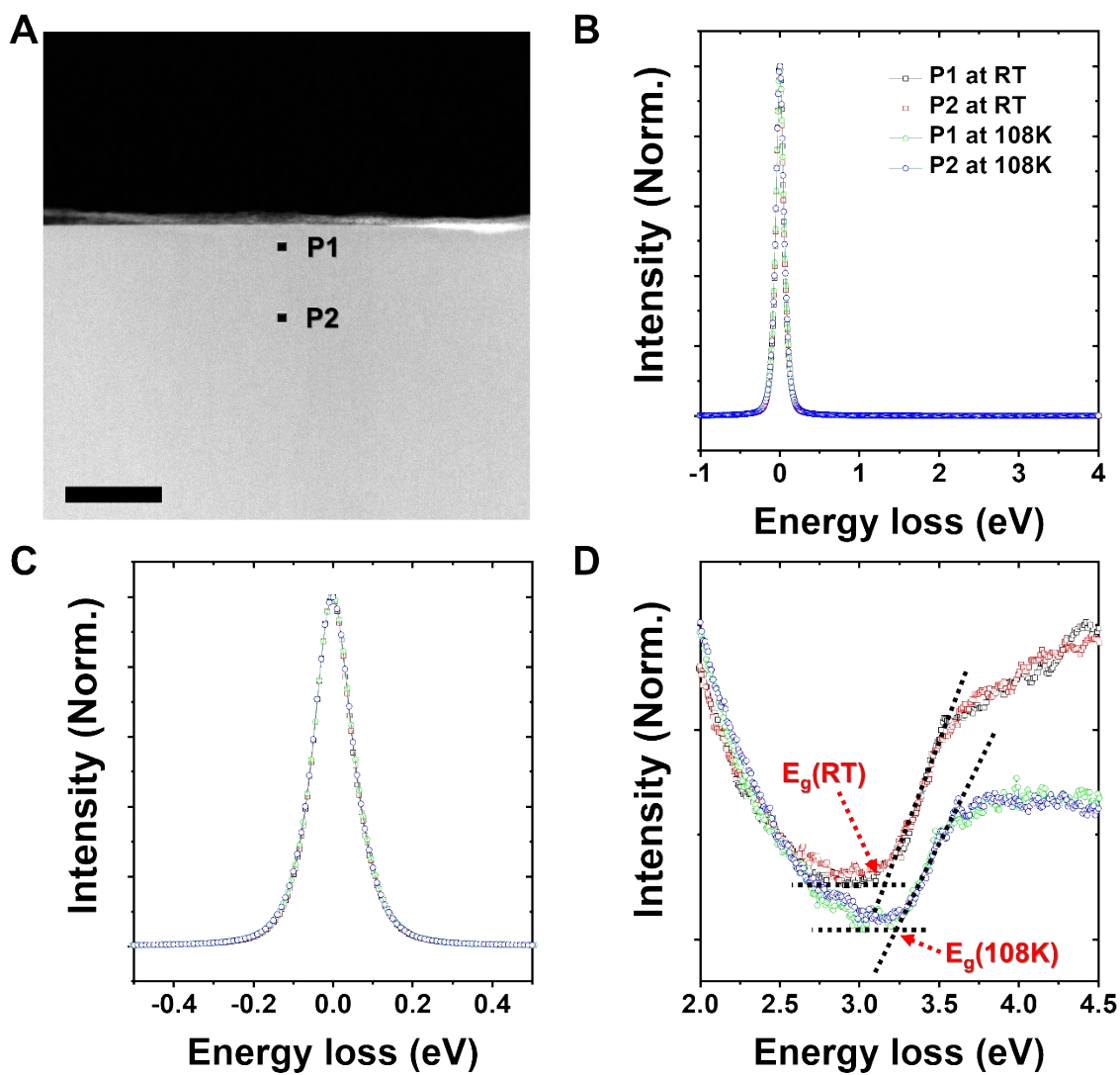
Figure S13. (a) HAADF–STEM images of GaN and the corresponding (b) low-loss EELS spectra at room temperature (open squares) and 108 K (open circles) at marked points of (a). (c,d) Enlarged spectrum of (b). Scalebar is 100 nm.
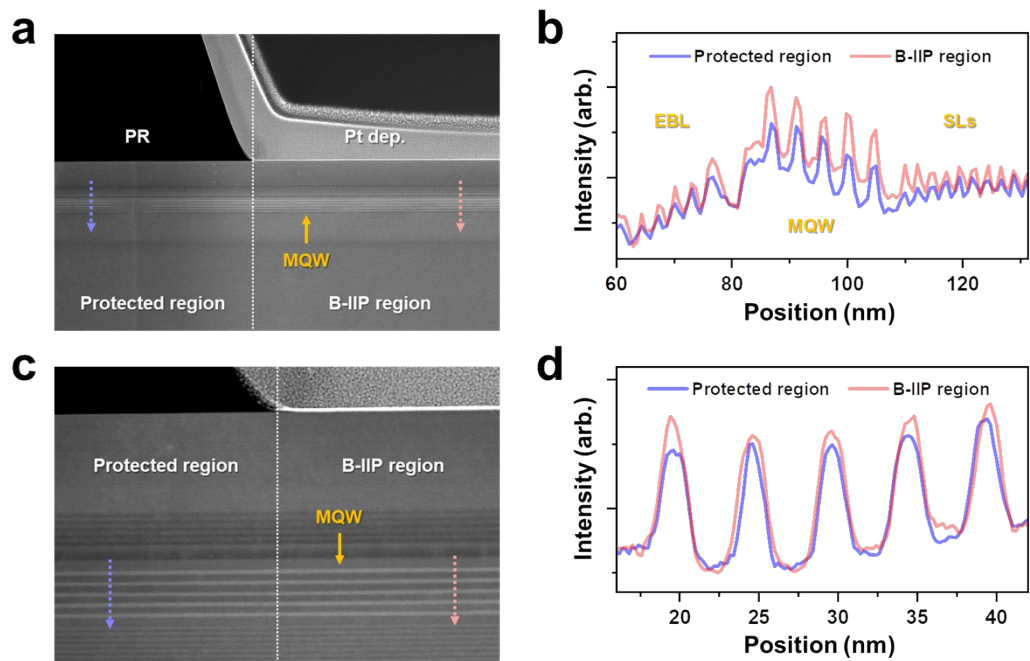
Figure S14. (a-b) STEM-HAADF images and corresponding (c-d) the intensity line profiles.
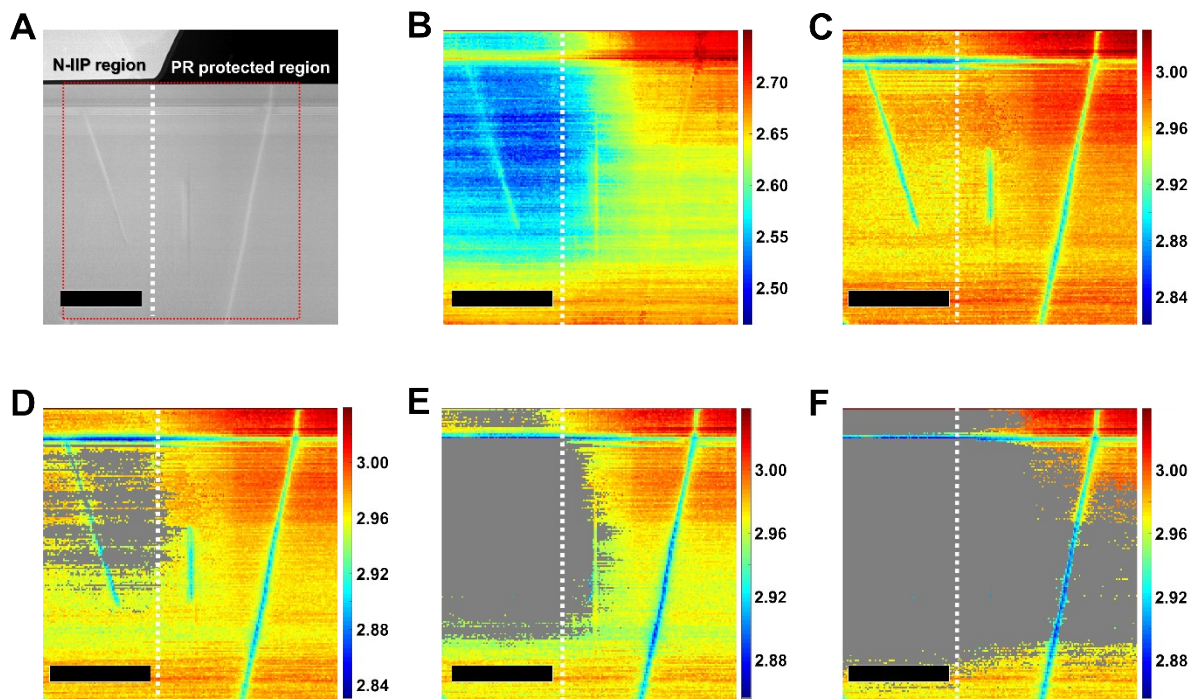
Figure S15. Reconstruction of the hyperspectral map using bandgap and defect-state energy maps of N-IIP InGaN-based LED device. (a) HAADF–STEM images and the corresponding (b) defect-state energy, including the (c) bandgap maps. Hyperspectral maps are reconstructed such that the defect-state energy map overlaps that of the bandgap in the range of the minimum values of (d) E_d = 2.34, (e) 2.39, and (f) 2.44 eV. All scale bars are 200 nm.
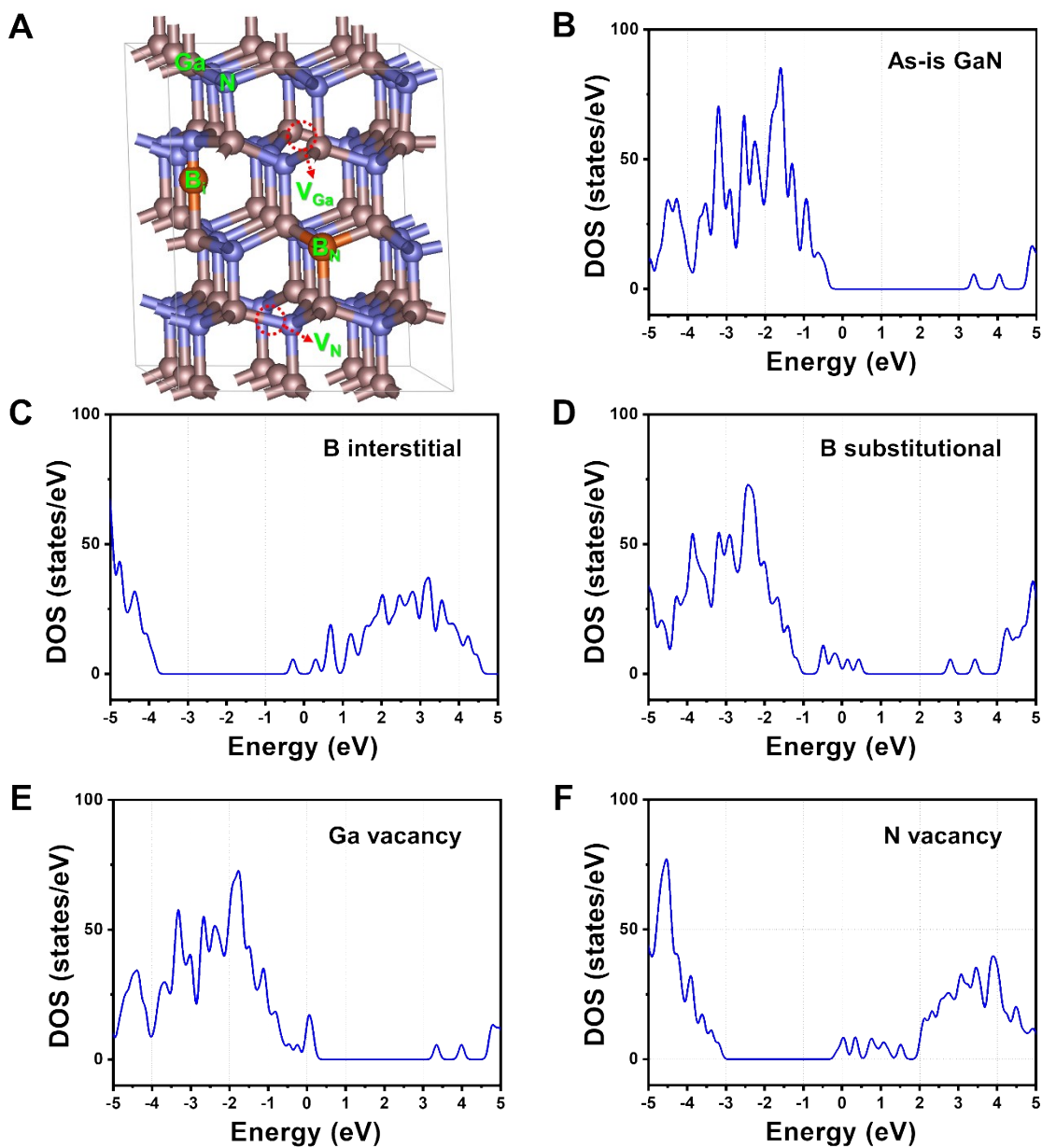
Figure S16. Theoretical total DOS for perfect crystal (As-is) GaN with point defects. (a) Atomic structure of GaN with point defects. The total DOS plots of (b) (As-is) GaN with (c) B interstitial, (d) B substitutional, (e) Ga vacancy, and (f) N vacancy.
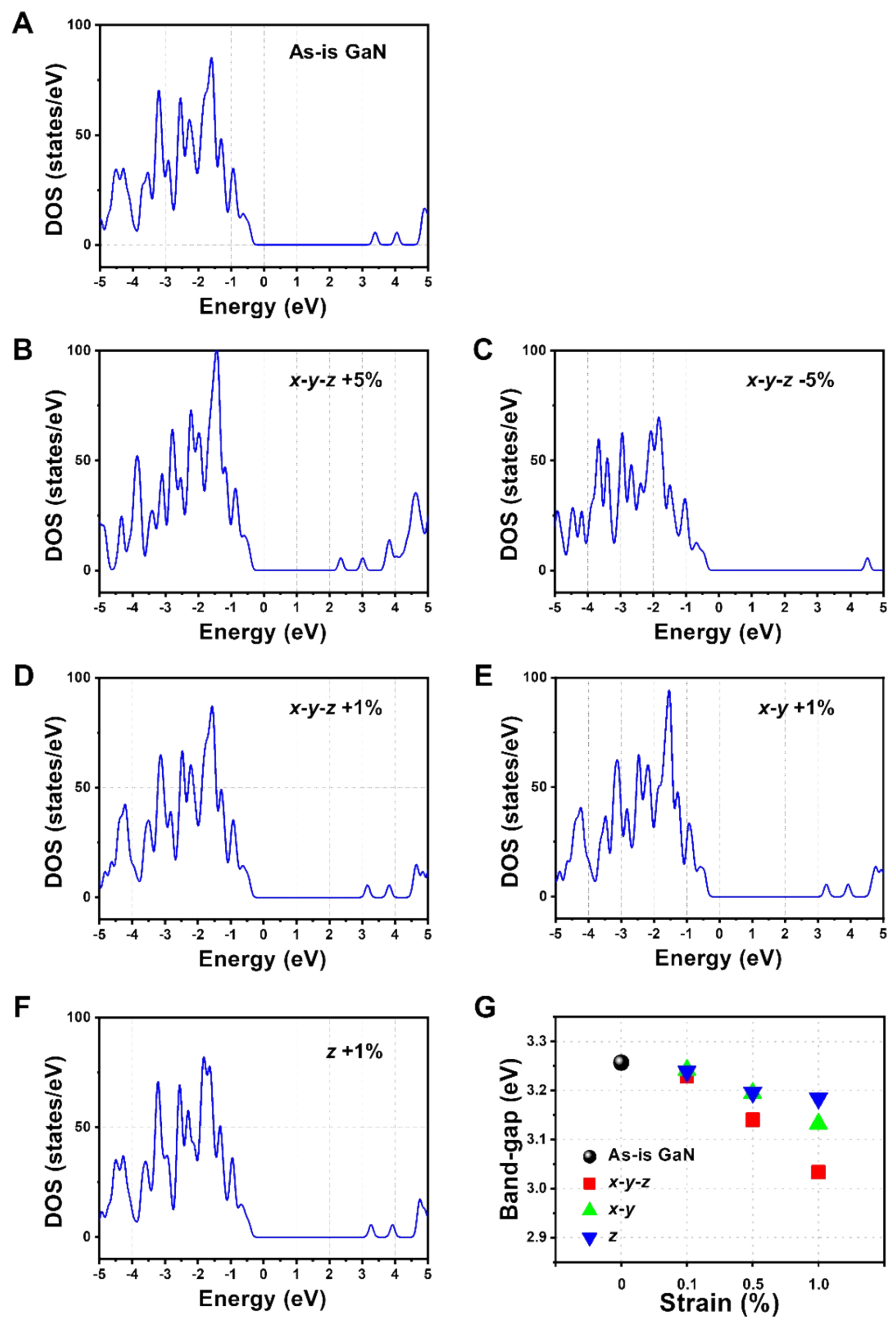
Figure S17. Theoretical total DOS for the perfect crystal (As-is) GaN with lattice strains. The total DOS plots of (a) As-is GaN, (b) +5% (tensile), (c) −5% (compressive) strained in the x-, y-, and z-axes, (d) +1% strained in the x-, y-, and z-axes, (e) in the x- and y- axes, and (f) only in z-axis. (g) Bandgap vs. strain.
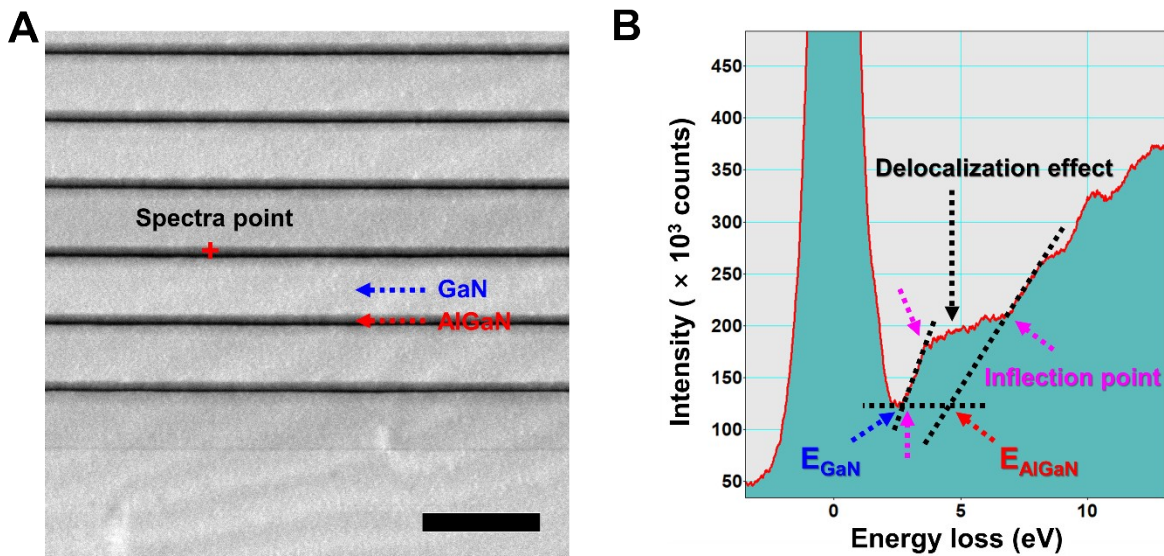
21

Figure S18. (a) HAADF–STEM image and the corresponding (b) low-loss EELS spectra of the AlGaN layer in the multilayer AlGaN/GaN system. Scalebar is 10 nm.

Table S1. List of cell sizes for DOS calculations

Cell size[a]	X (Å)	Y (Å)	Z (Å)
As-is GaN	9.74131	9.74132	10.56524
x-, y-, z-axis, +0.1 %	9.75106	9.75106	10.57581
x-, y-, z-axis, +0.5 %	9.79002	9.79003	10.61807
x-, y-, z-axis, +1.0 %	9.83873	9.83873	10.67089
x-, y-, z-axis, +5.0 %	10.22839	10.22839	11.09350
x-, y-, z-axis, -5.0 %	9.25425	9.25425	10.03698
x-, y-axis, +0.1 %	9.75106	9.75106	10.56524
x-, y-axis, +0.5 %	9.79002	9.79003	10.56524
x-, y-axis, + 1.0 %	9.83873	9.83873	10.56524
z-axis, +0.1 %	9.74131	9.74132	10.57581
z-axis, +0.5 %	9.74131	9.74132	10.61807
z-axis, +1.0 %	9.74131	9.74132	10.67089

[a] The calculated cell size is 3 × 3 × 2 multiplied by the unit cell of GaN (a = 3.24710, b = 3.24710, and c = 5.28265).

23

References

S1. Z. Huang Z, et al., *AIP Adv.,* 2019, **9**, 115106. DOI: 10.1063/1.5120324.

S2. J. F. Ziegler, M. D. Ziegler, J. P. Biersack, *Nucl. Instrum. Meth. Phys. Res. B,* 2010, **268**, 1818-1823. DOI: 10.1016/j.nimb.2010.02.091.

S3. S. Schön, M. Haiml, U. Keller, *Appl. Phys. Lett.,* 2000, **77**, 782–784. DOI: 10.1063/1.1306917.